

Article

# Methodology for Comprehensive Comparison of Energy Harvesting Shock Absorber Systems

Carlos Gijón-Rivera <sup>1,2</sup> and José Luis Olazagoitia <sup>1,\*</sup> 

<sup>1</sup> Industrial Engineering and Automotive Department, Universidad de Nebrija, Campus de la Dehesa de la Villa, Calle Pirineos, 55, 28040 Madrid, Spain; cgijonr@alumnos.nebrija.es

<sup>2</sup> Escuela de Ingeniería y Ciencias, Tecnológico de Monterrey, Ave. Eugenio Garza Sada 2501, Monterrey NL 64849, Mexico

\* Correspondence: jolazago@nebrija.es

Received: 12 October 2020; Accepted: 17 November 2020; Published: 21 November 2020



**Abstract:** In recent years, there has been a lot of work related to Energy Harvesting Shock Absorbers (EHSA). These devices harvest energy from the movement of the vehicle's shock absorbers caused by road roughness, braking, acceleration and turning. There are different technologies that can be used in these systems, but it is not clear which would be the best option if you want to replace a conventional shock absorber with an EHSA. This article presents a methodology to compare the performance of different EHSA technologies that can replace a shock absorber with a given damping coefficient. The methodology allows to include different analysis options, including different types of driving cycles, computer vehicle models, input signals and road types. The article tests the methodology in selecting the optimal EHSA technology for a particular shock absorber and vehicle, optimizing at the same time energy recovery. In addition, a study of parameters in each type of technology is included to analyze its influence on the final objective. In the example analyzed, the EHSA technology with a rack and pinion system turned out to be the best. The proposed methodology can be extrapolated to other case studies and design objectives.

**Keywords:** EHSA; energy harvesting; shock absorber; methodology; damping coefficient; design

## 1. Introduction

Given the paradigm of the world's increasing energy needs and environmental problems due to pollution, reducing energy consumption, or improving the efficiency of existing or new systems is a must. One of the sectors with the most opportunities for improvement is transport, which since 1980 has been the largest consumer of fuel, and also the largest generator of greenhouse gases.

For light vehicles, regulations are stricter, and this has led to a trend to bring cars with higher fuel efficiency and lower emissions to the market [1]. This applies to electric, hybrid and internal combustion vehicles. Electric and hybrid vehicles are more efficient than internal combustion vehicles, with energy losses from the drive system of 15 to 20%, compared to 64 to 75% for the gasoline engine. In general, electric vehicles are 60–73% efficient, depending on the driving cycle [2].

The performance of cars can be improved by recovering the energy they waste. There are different technologies such as: Kinetic Energy Recovery Systems (KERS), Energy Harvesting Shock Absorber Systems (EHSA) and Waste Heat Recovery Units.

The goal is to increase the effectiveness and life of electric and hybrid vehicle batteries to reduce high costs. Energy recovery in vehicles can improve their performance and cover different electrical power needs within the vehicle, from feeding back the vehicle battery to covering the needs of specific sensors without the need for additional wiring.

The European Community reports that the transport sector accounts for at least 25% of greenhouse gas emissions and is the main cause of pollutant emissions in urban areas [3]. In this sense, one of the aspects that most impact the current energy crisis is the increase in internal combustion motor vehicles that base their operation on the use of fossil fuels. Therefore, there is a great area of opportunity in research and technological development of automotive applications that help improve energy efficiency and reduce pollutant emissions from vehicles using energy recovery systems.

As far as electric vehicles are concerned, the technological solution proposals have focused on the use of hybrid and electric vehicles and on the study of energy recovery systems to incorporate energy into the battery and thus improve the vehicle's autonomy and reduce greenhouse gas emissions.

Although the technological proposals are not recent, the search for energy efficiency in automotive suspension systems is a current research field with wide possibilities for innovation. Energy recovery systems in shock absorbers are systems that allow obtaining useful energy dissipated in the form of heat in conventional hydraulic shock absorbers. Ideally, these EHSA systems should replace the current ones, allowing energy recovery, without altering the vehicle dynamics; this means maintaining the comfort and stability of the vehicle. However, the developments found have focused more on the technologies and capabilities of the EHSA systems developed, rather than on the possibility of replacing conventional shock absorbers with others that provide the same damping as the initial ones. Therefore, it is a technology still under development and with few functional prototypes.

In the last few years, EHSA energy recovery dampers have received special attention in the specialized literature. It has been shown that the energy recovered by these systems can be relevant in global energy computation. According to Zuo et al. [4], the range of energy recovered in EHSA systems is from 100 to 400 W, when the power consumed by a cell phone is 1 W.

EHSA systems can be classified into different types, depending on the technology used for energy recovery. There are EHSA systems based on piezoelectricity [5,6], which have not been widely developed perhaps because they focus on small displacements and the energy that can be recovered is considerably less than that provided by electromagnetic systems. For this reason, electromagnetic systems are the most documented and used to date in the research presented.

Electromagnetic dampers can be subdivided into linear [7,8] and rotational [9,10]. The first ones represent the ideal solution due to the use of the oscillatory linear movement in a direct way. However, the energy recovered in electromechanical systems depends directly on the speed generated in the system and linear systems do not usually present an extension of linear motion, which makes the generation of energy limited. In addition, the cost of weight and winding required for operation, together with the fact that the useful travel of the suspension is usually not very high, means that its use has not been the preferred option in research work [11]. For this reason, many authors have opted for EHSA rotational electromagnetic. The latter are the ones that have made the most progress due to the lower total weight of the set, compactness, and simplicity of assembly. Within these rotational systems, there are several solutions to convert the translation movement from the suspension to the rotation movement of the generator that will provide the energy recovery: rack and pinion transmission [10], ball screw transmission [12], hydraulic transmission [6], two-link transmission (Two-leg mechanism or Algebraic Screw Linkage transmission) [13] and cable transmission [14]. Finally, these systems may or may not include a motion rectifier [12], which means that the rotational movement always acts in one direction despite having oscillating movement of the shock absorber.

The EHSA study was heterogeneous and many types of models representing the vehicle suspension were presented. According to the literature, we find EHSA systems applied to various models of different degrees of freedom (DOF). F. Khoshnoud et al., it shows a 2 DOF model [15] and includes the calculation of calculated energy in pitch and roll modes. Comparing the theoretical and experimental results with an offset between the dampers, they obtain an average of 984 W, 841 W, 876 W recovered energy for the vertical movements, pitch, and roll modes.

On the other hand, Models with 4 DOF have been reported, simulating pitch and roll movements, in addition to the vertical displacement, we identify C. Wei et al. [16] with an instantaneous power of

64 W for the front shock absorber and 40 W for the rear one, the work of Lafarge et al. [17] with a 4 DOF model, recovering 40 W average. Models with 6 DOF that capture vertical displacement and pitch mode of both the sprung mass and the seat with an average recovered energy of 31.63–55.39 W have been reported by Nakano et al. [18]. Finally, full vehicle models, with 9 DOF and 24.75 W recovery for 60 km/h are reported by Mi et al. [19] and 480 W for 90 km/h with 7 DOF by Pham et al. [20]. The work reported by Abdelkareem et al. [21] showed a model of 7 DOF with energy recovery of 51 W for a speed of 36 km/h, 100 W for a speed of 72 km/h, and 151 W with a speed of 108 km/h.

#### *Use of Driving Cycles in the Analysis of EHSA Systems*

In the simulation of the previous models, the researchers use different techniques to validate their developments. In some cases, simple signals are used. Sometimes, regulated driving cycles are selected. In other cases, signals recorded directly from vehicles are applied. The driving cycles are usually applied under standardized laboratory conditions to new vehicles before they enter a market. They consist of a sequence of events of braking and acceleration, attached to typical real road conditions. These tests are performed to determine the fuel consumption and CO<sub>2</sub> emissions of internal combustion engine vehicles [22,23].

To evaluate the performance of energy recovery systems, sinusoidal functions [24,25] can be used to random signals of variable amplitude to simulate standardized driving events from different environments and road types. Several driving cycles have been used in the energy recovery study of EHSA systems that provide better input information than harmonic inputs can.

The use of drive cycles to evaluate EHSA performance began in 2016, using the New European Driving Cycle (NEDC) in a 3-degree of freedom model [26]. They used 10 different cycles, 5 of which were city cycles. The road roughness profile was included in a half vehicle model with 4 DOF [27] in the work of M. Abdelkareem et al. [21]. They conclude that steady-state driving cycles (composed of periods of constant acceleration and deceleration, NEDC, EUDC (Extra Urban Driving Cycle) at high speeds can recover more energy than transient state speed cycles (composed of a wide range of speeds and accelerations Worldwide Harmonised Light Vehicles Test Procedure (WLTP), FTP (Federal Test Procedure), HWFET (Highway Fuel Economy Test). They also add to the pitch movement a speed delay function between the rear and front wheels using a 7 DOF model.

M. Abdelkareem et al. [28] test 10 driving cycles (HDUDD, NYCC, LA92, US06, SC06, CUEDC, IM240, J1015, RTS95, CSC) that were applied with random road profiles at different speeds and under two driving condition (aggressive and non-aggressive). They also include the loaded and unloaded car variant in a 6-degree of freedom half truck model. Within the 6 degrees of freedom, pitching is included.

On the other hand, road profile modeling has been used extensively to simulate the roughness of road profiles and to obtain an estimate of the recoverable energy in them [29–31]. Road roughness has a fundamental influence on the energy that can be recovered in EHSAs. In theoretical roads without any roughness, the energy recovery would be limited to the pitching or turning movement of the vehicle. The amount of energy that is possible to recover is increased in roads with higher roughness as shown in the work performed by Lincoln Bowen and Yuxin Zhang [32,33] where they compare different types of roads (A, B, C, and D) at different speeds and obtain the power. In the same way, mechanical efficiency is reduced by increasing the input frequency as shown by Zhongjie Li [9]. From these works, it can be concluded that the use of standardized driving cycles is a good approximation to estimate the energy recovered, which can be improved by including the vertical dynamics of the vehicle and the turns.

To consider the EHSA energy recovery calculation of a complete vehicle it is important to ensure that pitch and roll capabilities are included in the vehicle model. This makes it interesting to include the lateral dynamics as well as the vertical and longitudinal dynamics of the vehicle. Published works on the subject sometimes include a trajectory profile delay function on each of the wheels, so that it causes rotations in the vehicle. If these delays are included in driving cycle tests (such as the WLTP), the simulation of recoverable energy would be closer to reality.

In summary, after reviewing the articles published on the design, simulations, development and testing of EHSA systems, it can be concluded that there is a great heterogeneity of studies. There are different technologies applicable to EHSAs. In addition, the computer models used can include 2 DOFs or reach up to 9 DOFs. The models can be simulated in different types of roads with different roughness, at different speeds or different driving cycles, incorporating in the model the vertical and lateral dynamics. At the test level, they can be applied from basic sinusoidal signals to signals acquired directly from the vehicle instrumentation. This diversity in the design, simulation, testing and validation makes it almost impossible to have a clear idea of the performance of one EHSA system compared to the others. However, this comparison is essential if we are to take a leap forward and try to make this technology viable for the manufacture of functional prototypes.

The motivation for this article is the difficulty that currently exists to contextualize and put into a common frame of reference all the data available in the relevant literature. From the point of view of an EHSA system designer it is desirable to be able to compare and know which technology is the best, and under which conditions it is so. It is also important to know which parameters are the most sensitive and most influential in the design. For this reason, this paper proposes a methodology that allows the comparison of results obtained through different technologies and EHSA designs. With this methodology, the comparative criteria of different EHSA prototypes for energy recovery are standardized, in a structured and agile way, based on different driving cycle conditions, different types of roads (both urban and highway), and with different driving parameters and vehicle characteristics. In this way, different EHSA systems can be compared with each other on the basis of a standardized working environment. This methodology for the analysis and comparison of EHSA systems aims at facilitating the design of an EHSA system to choose between the different available technologies and their design parameters, comparing them with each other under consistent and comparable validation conditions.

The novelty of this article, therefore, aims to respond to this challenge by presenting an inclusive methodology and a unique integrative tool, which can take into account within it every one of the variables that have been discussed (vehicle models, types of EHSA, driving cycles, road profiles, etc.) that the designer can choose to make the comparison. For this purpose, a new global methodology is proposed and its functionality is presented through a case study in which three of the technologies currently used in the design of rotational electromagnetic EHSA systems are compared.

With the idea of being more inclusive in terms of the degrees of freedom that can be modelled, we will use a complete vehicle model that allows for the inclusion of movements such as pitching and rolling, movements that are normally experienced in real conditions.

The article is distributed as follows. In Section 2, the methodology used in the work is shown, the simulation of the mathematical model is used with the incorporation of the WLTP driving cycle, going deeper into the modeling of turnings., In Section 3, the methodology applied is shown in the comparison of the different EHSA systems. Section 4 focuses on showing the results and discussions obtained from the three systems analyzed, and the parameters of greater effect selected, tested in the complete vehicle model with 7 DOF. Section 5 concludes from the results obtained and, finally, presents recommendations for future work.

## 2. Materials and Methods

The methodology goes beyond establishing the same conditions for the modeling of all EHSA systems. In this way, four different stages were established (Figure 1).

**Input.** In this first stage, the selected standardized driving cycles can be combined with the selected road roughness. The modeling includes the vehicle model and parameters such as: spring stiffness of the EHSA system, masses, and wheel stiffness. Finally, the user can select the preferred EHSA technology to be used.

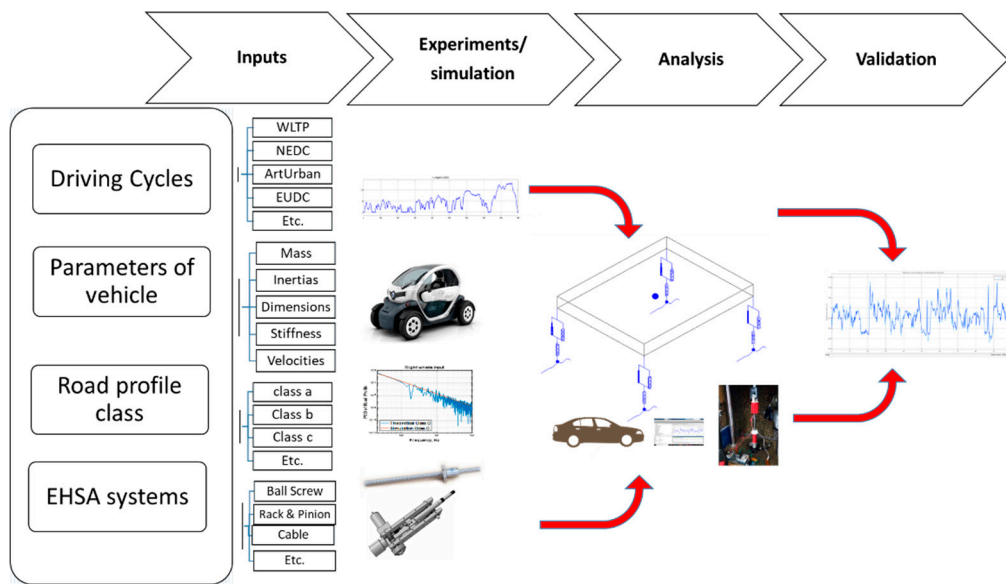


**Figure 1.** Proposed methodology for the analysis of Energy Harvesting Shock Absorber Systems (EHSA) systems with driving cycles.

**Experiments/Simulation.** To reach this stage it is important to identify the most effective parameters of the EHSA system that have the greatest impact on energy harvesting. Once the inputs are available, the experiments or the vehicle model for the simulations can be performed.

**Analysis.** At this stage, all the necessary iterations are carried out to obtain reliable, consistent, and congruent results.

**Validation.** At this later step, it is possible to compare, under the same design and validation conditions, the different EHSA technologies selected for the design.

### 2.1. Suspension and Vehicle Models

In this case, a full 7 DOF car model was chosen, which will be able to include in the energy recovery calculation vertical, pitching and rolling vehicle movements. The mathematical model is described in Figure 2.

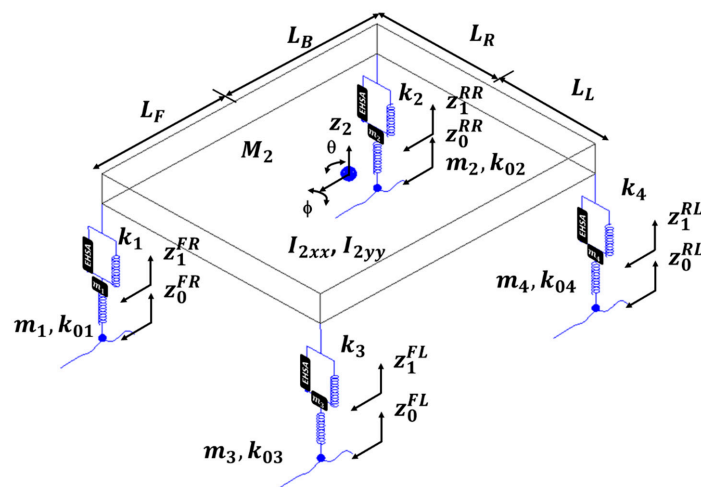


**Figure 2.** Full vehicle model with 7 degrees of freedom (DOF) where  $Z_1^{FL}$ ,  $Z_1^{FR}$ ,  $Z_1^{RL}$ ,  $Z_1^{RR}$ ,  $Z_2$ ,  $\theta$ , and  $\varphi$  represent the DOF of the system and  $Z_1$  represents the vertical displacements of the shock absorber,  $Z_2$  represents the vertical displacement of the sprung mass,  $\theta$  represents the pitch mode,  $\varphi$  represents the roll mode.

For demonstrative purposes, mass and rigidity parameters are simplified as follows:  $m_1 = m_2 = m_3 = m_4$ ,  $k_1 = k_2 = k_3 = k_4$ .

Equations for the complete vehicle are deducted from Newton's second law:  $\sum ma = F$  at sprung mass

$$M_2\ddot{z}_2 = k_1(z_2 - z_1^{FL} + L_F\theta + L_L\varphi) + k_3(z_2 - z_1^{FR} + L_F\theta - L_R\varphi) + k_2(z_2 - z_1^{RL} - L_F\theta + L_L\varphi) + k_4(z_2 - z_1^{RR} - L_F\theta - L_L\varphi) + C_{EHSA1}(\dot{z}_2 - \dot{z}_1^{FL} + L_F\theta + L_L\varphi) + C_{EHSA3}(\dot{z}_2 - \dot{z}_1^{FR} + L_F\theta - L_R\varphi) + C_{EHSA2}(\dot{z}_2 - \dot{z}_1^{RL} - L_F\theta + L_L\varphi) + C_{EHSA4}(\dot{z}_2 - \dot{z}_1^{RR} - L_F\theta - L_L\varphi) \quad (1)$$

$\sum I\theta = T$  on the sprung mass (pitch)

$$I_{2xx}\ddot{\theta}_2 = L_Fk_1(z_2 - z_1^{FL} + L_F\theta + L_L\varphi) + L_Fk_3(z_2 - z_1^{FR} + L_F\theta - L_R\varphi) + L_Bk_2(z_2 - z_1^{RL} - L_F\theta + L_L\varphi) + L_Bk_4(z_2 - z_1^{RR} - L_F\theta - L_L\varphi) + L_FC_{EHSA1}(\dot{z}_2 - \dot{z}_1^{FL} + L_F\theta + L_L\varphi) + L_FC_{EHSA3}(\dot{z}_2 - \dot{z}_1^{FR} + L_F\theta - L_R\varphi) + L_BC_{EHSA2}(\dot{z}_2 - \dot{z}_1^{RL} - L_F\theta + L_L\varphi) + L_BC_{EHSA4}(\dot{z}_2 - \dot{z}_1^{RR} - L_F\theta - L_L\varphi) \quad (2)$$

$\sum I\varphi = T$  in the sprung mass (roll)

$$I_{2yy}\ddot{\varphi}_2 = L_Lk_1(z_2 - z_1^{FL} + L_F\theta + L_L\varphi) + L_Rk_3(z_2 - z_1^{FR} + L_F\theta - L_R\varphi) + L_Lk_2(z_2 - z_1^{RL} - L_F\theta + L_L\varphi) + L_Bk_4(z_2 - z_1^{RR} - L_F\theta - L_L\varphi) + L_FC_{EHSA1}(\dot{z}_2 - \dot{z}_1^{FL} + L_F\theta + L_L\varphi) + L_FC_{EHSA3}(\dot{z}_2 - \dot{z}_1^{FR} + L_F\theta - L_R\varphi) + L_BC_{EHSA2}(\dot{z}_2 - \dot{z}_1^{RL} - L_F\theta + L_L\varphi) + L_RC_{EHSA4}(\dot{z}_2 - \dot{z}_1^{RR} - L_F\theta - L_L\varphi) \quad (3)$$

To exemplify the car model, the parameters of a compact car was included (Renault Twitzy 45, shown in Table 1).

**Table 1.** Data on the vehicle used for full car model.

Parameters	
$M_2$ (Kg)	650
$m_1$ (Kg)	24
$I_{2xx}$ (Kgm <sup>2</sup> )	77
$I_{2xx}$ (Kgm <sup>2</sup> )	296
$k_1$ (N/m)	10,286
$k_{01}$ (N/m)	106,111
$L_L = L_R$ (mm)	596
$L_F$ (mm)	1110
$L_B$ (mm)	1227



## 2.2. Selection of EHSA Technology

As an example, in this work, three of the most used EHSA systems in the literature were selected: ball screw, rack and pinion, and cable transmission [14].

The EHSA study is based on the methodology proposed by L. Bowen et al. [32] for the analysis of these EHSA systems. Figure 3 shows the DC motor model used in the three selected EHSA systems.

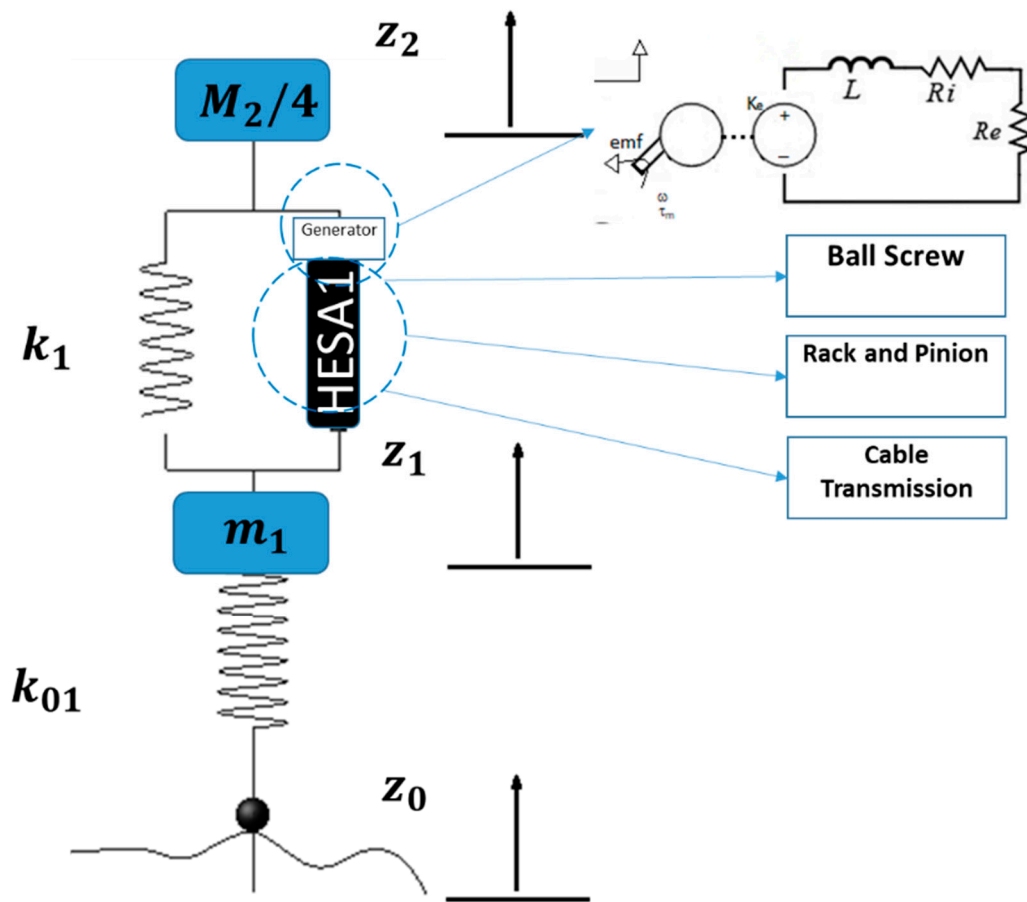


Figure 3. Quarter Vehicle Model.

From the model of the DC motor the relation between the current of the conductor  $i$  of the circuit, the constant of the torque  $k_i$  and the moment is established by

$$\tau_i = k_i i \tag{4}$$

On the other hand, applying Newton's second law

$$\tau_g - \tau_i = J_g \frac{d\alpha_g^2}{dt} \tag{5}$$

where  $\tau_g$  is the generator input torque;  $J_g$  is the motor inertia;  $\alpha_g$  is the spindle rotation.

From the lows Kirchorff's voltage laws:

$$U_{emf} - L \frac{di}{dt} - iR = 0 \tag{6}$$

where  $U_{emf}$  is the counter electromotive force that depends directly on the speed change and  $k_e$  represents the counter electromotive voltage constant

$$U_{emf} = k_e \frac{d\alpha_g}{dt} \tag{7}$$

By simplifying the above equations and applying Laplace's transform.

$$k_e \frac{dq}{dt} = \frac{L}{k_i} \left[ \frac{d\tau_g}{k_i dt} - J_g \frac{d^3 \alpha}{dt^3} \right] + \frac{R}{k_i} \left[ \tau_g - \frac{J_g d^2 \alpha}{dt^2} \right] \quad (8)$$

Sorting and clearing up the torque in Laplace's domain:

$$T_g = J_g A s^2 + c_g A s + k_g A \quad (9)$$

Grouping in equivalent factors,  $C_g$  and  $K_g$  are expressed as:

$$C_g = \frac{K_i K_e R}{R^2 + L^2 \omega^2} \quad (10)$$

$$K_g = \frac{K_i K_e L \omega^2}{R^2 + L^2 \omega^2} \quad (11)$$

### 2.2.1. Ball Screw Model

The Ball-Screw Energy Harvesting Shock Absorber (BS-EHSA) system, which is defined as a linear actuator that transforms the linear movement into angular, is characterized by handling pitch angles from 1 to 10 degrees, friction coefficients from 0.01 to 0.003 that accounts for efficiencies above 90% [34].

The ball screw system is formed when the end of the screw is connected to the electric generator, while the nut is connected to the shock absorber. These systems are often used because they represent a simple solution related to the number of components connected and they are ease of assembly and robust. In Figure 4, the generator is coupled to the spindle, where  $\tau_g$  is the generator torque and  $\alpha$  is the angular displacement.

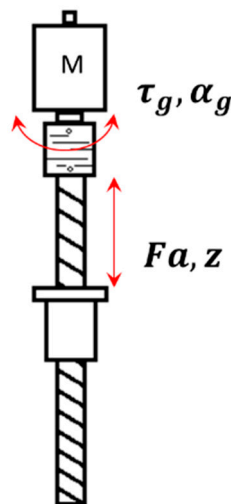


Figure 4. Ball screw sketch.

Some disadvantages of this technology is that some mechanical failures might occur, such as the possibility of reaching critical speed rotation, the wear of balls and tracks and reduction of system life due to fatigue in components depending on the maximum load and speed determined by the manufacturer.

Considering the efficiency, the inertia, and the ratio of the dynamic equations of the ball screw in the transformation from linear to angular motion we have:

$$\eta_{bs} F_a \dot{z} = J_s \dot{\alpha}_s \ddot{\alpha}_s + \tau_g \dot{\alpha}_g \quad (12)$$

$$\alpha_s = \alpha_g \tag{13}$$

The relationship between the relative displacement  $z$  and angular displacement  $\alpha_s$  of Ball Screw and lead:

$$z = \frac{\alpha_s l}{2\pi} \tag{14}$$

where  $z$  represents the axial displacement of a nut on the spindle and  $l$  is the lead. Derivating and clearing  $\tau_g$ .

$$\tau_g = J_g \ddot{\alpha}_g + c_g \dot{\alpha}_g + k_g \alpha_g \tag{15}$$

where  $z$  represents the axial displacement of a nut on the spindle and  $l$  is the lead.

$$m_{eq} = (2\pi)^2 \frac{J_g + J_s}{\eta_{bs} l^2} \tag{16}$$

$$c_{eq} = (2\pi)^2 \frac{K_i K_e R}{l^2 \eta_{bs} (R^2 + L^2 \omega^2)} \tag{17}$$

$$k_{eq} = (2\pi)^2 \frac{K_i K_e L_i \omega^2}{l^2 \eta_{bs} (R^2 + L^2 \omega^2)} \tag{18}$$

and where  $F_a$  represents the input force of the path or excitation.

### 2.2.2. Rack and Pinion System

The rack and pinion drive system (Figure 5) is very robust mechanically, although it has the disadvantage of gear backlash and therefore limited wear and tear and fatigue durability.

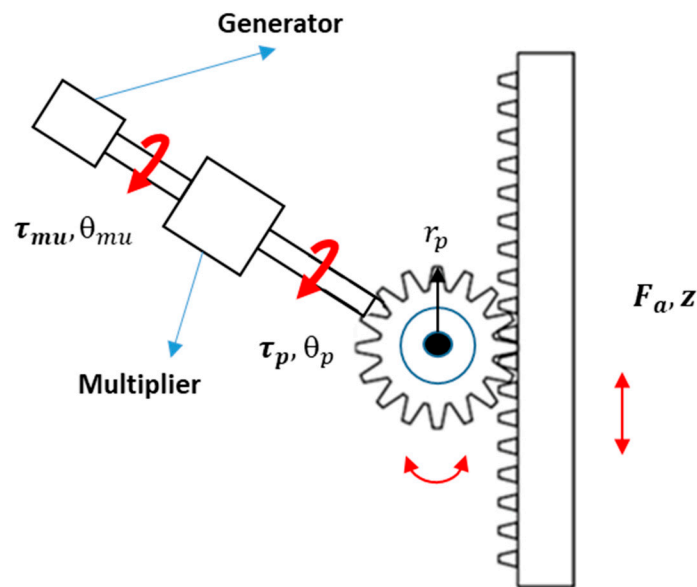


Figure 5. EHS component diagram rack and pinion.

By using the same generator for all EHS systems, the formulation obtained in the Equations (15)–(18) ball screw system can be used.

Making a balance of power on the pinion shaft,

$$n_p F_a \dot{z} = \tau_p \dot{\theta}_p + J_p \ddot{\theta}_p \tag{19}$$

The balance on the gearbox shaft.

$$n_{mu}\tau_p\dot{\theta}_p = \tau_{mu}\dot{\theta}_{mu} + J_{mu}\ddot{\theta}_{mu}\dot{\theta}_{mu} \tag{20}$$

$$\tau_{mu} = J_m\ddot{\theta}_{mu} + c_m\dot{\theta}_{mu} + k_m\theta_{mu} \tag{21}$$

From the relationship of linear and rotational movement between rack and pinion,

$$\dot{\theta}_p = \frac{\dot{z}}{r_p} \tag{22}$$

In Equation (22),  $r_p$  represents the pinion radius. The ratio of the angular displacement of the gearbox between the input and output.

$$k_{mu} = \frac{\theta_{mu}}{\theta_p} \tag{23}$$

Substituting in Equation (19) and grouping the terms  $M_{eqRP}$ ,  $C_{eqRP}$ ,  $K_{eqRP}$ .

$$M_{eqRP} = \frac{(J_{mu} + J_m)k_{mu}^2}{n_p n_{mu} r_p^2} + \frac{J_p}{n_p r_p^2} \tag{24}$$

$$C_{eqRP} = \frac{(K_{mu}^2 K_e K_i (Re + Ri))}{n_p n_{mu} r_p^2 ((Re + Ri)^2 + L_i^2 \omega^2)} \tag{25}$$

$$K_{eqRP} = \frac{(K_{mu}^2 K_e K_i L_i (Re + Ri))}{n_p r_p^2 ((Re + Ri)^2 + L_i^2 \omega^2)} \tag{26}$$

### 2.2.3. Cable Driving Transmission System

The third technology for the comparison is the CD-EHSA (Cable Dynamics Energy Harvesting Shock Absorber [5], an innovative system that has the advantage of having a good ratio between rigidity and weight, good durability as shown in Figure 6.

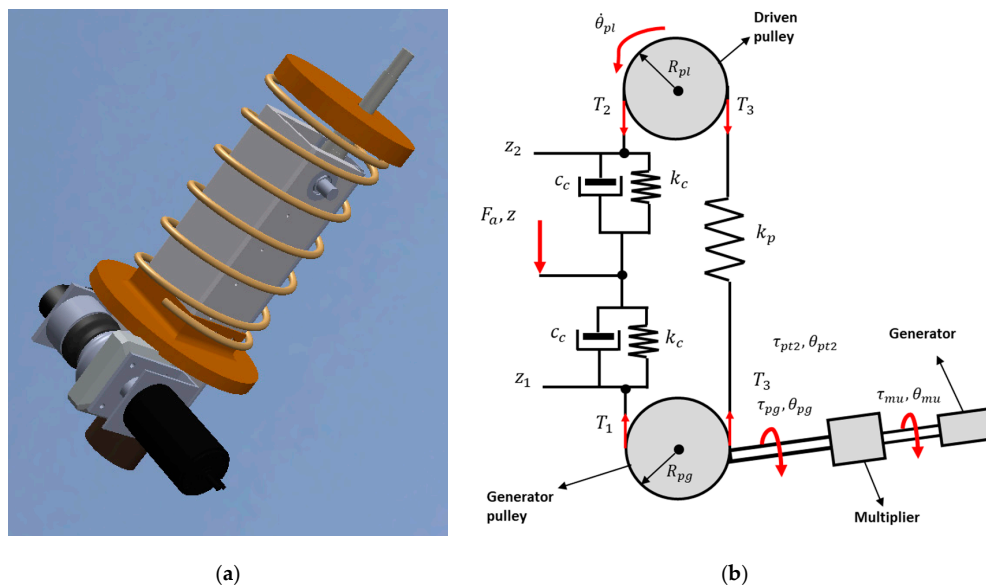


**Figure 6.** (a) Present a CAD model from EHSA cable transmission, (b) The derivation of the cable model equations from the free body diagram.

The equations for this model are shown below:  
Based on the balance of forces condition in the cable,

$$F_a = T_2 - T_1 \quad (27)$$

Balancing energy on the pulley in the drive pulley,

$$n_{pg}(T_2 - T_1)R_{pg}\dot{\theta}_{pg} = \tau_{pg}\dot{\theta}_{pg} + J_{pg}\ddot{\theta}_{pg}\dot{\theta}_{pg} \quad (28)$$

$$T_1 = k_c(z_1 - z) + c_c(\dot{z}_1 - \dot{z}) \quad (29)$$

$$T_2 = k_c(z - z_2) + c_c(\dot{z} - \dot{z}_2) \quad (30)$$

$$T_3 = k_p(z_2 - z_2) + T_p \quad (31)$$

$$(T_2 - T_1)R_{pl} = J_{pl}\ddot{\theta}_{pl} \quad (32)$$

$$\dot{\theta}_{pl} = \frac{\dot{z}_2}{R_{pl}} \quad (33)$$

$$\dot{\theta}_{pg} = \frac{\dot{z}_1}{R_{pg}} \quad (34)$$

Making a balance of energy in the multiplier,

$$n_{mu}\tau_{pg}\dot{\theta}_{pg} = \tau_{mu}\dot{\theta}_{mu} + J_{mu}\ddot{\theta}_{mu}\dot{\theta}_{mu} \quad (35)$$

If we express the torque from the mass–spring–damper form,

$$\tau_{mu} = J_m\ddot{\theta}_{mu} + c_m\dot{\theta}_{mu} + k_m\theta_{mu} \quad (36)$$

The relationship between the input and output angular position of the gearbox.

$$k_{mu} = \frac{\theta_{mu}}{\theta_{pg}} \quad (37)$$

Clearing for  $F_a$ , and grouping the equivalent coefficients become

$$m_{eq}^* = \frac{1}{R_{pg}^2\eta_{pt1}\eta_{pg}} \left( J_{pt1} + J_{pg} + \frac{k_{pt}^2}{\eta_{pt2}} (J_{pt2} + J_{mu} - 2J_{mu}k_{mu}) + \frac{k_{mu}^2(J_{mu} + J_m)}{\eta_{mu}} \right) \quad (38)$$

$$c_{eq}^* = \frac{k_{mu}^2 k_{pt}^2 K_e K_i (R_e + R_i)}{R_{pg}^2 \eta_{pt1} \eta_{pg} \eta_{pt2} \eta_{mu} ((R_e + R_i)^2 + L_i^2 \omega^2)} \quad (39)$$

$$k_{eq}^* = \frac{k_{mu}^2 k_{pt}^2 K_e K_i L_i \omega^2}{R_{pg}^2 \eta_{pt1} \eta_{pg} \eta_{pt2} \eta_{mu} ((R_e + R_i)^2 + L_i^2 \omega^2)} \quad (40)$$

$$m_{eqCD} = \frac{(m_{eq}^* c_c^2 - m_{eq}^* 2k_c) \omega^2 + 2m_{eq}^* k_{eq}^* k_c + m_{eq}^* k_c^2 - c_{eq}^* 2k_c - k_{eq}^* c_c^2}{(k_{eq}^* + k_c - m_{eq}^* \omega^2)^2 + (c_{eq}^* + c_c)^2 \omega^2} \quad (41)$$

$$c_{eqCD} = \frac{(c_{eq}^* 2c_c + c_{eq}^* c_c^2 - 2k_{eq}^* c_c m_{eq}^*) \omega^2 + m_{eq}^* 2c_c \omega^4 + c_{eq}^* k_c^2 + c_c k_{eq}^* 2}{(k_{eq}^* + k_c - m_{eq}^* \omega^2)^2 + (c_{eq}^* + c_c)^2 \omega^2} \quad (42)$$

$$k_{eqCD} = \frac{k_{eq}^* k_c + k_{eq}^* k_c^2}{(k_{eq}^* + k_c - m_{eq}^* \omega^2)^2 + (c_{eq}^* + c_c)^2 \omega^2} \quad (43)$$

### 2.3. Driving Cycle

Once the EHSA technologies to be compared were chosen, the driving cycle for which the comparison will be made is selected. In this case, the Worldwide Harmonised Light Vehicles Test Procedure (WLTP) cycle was chosen, as it has become mandatory for car manufacturers since 2017, which is supposed to be closer to reality [35].

The cycle is divided into different classes. In this study, we will focus on class 3, which is further subdivided into two subclasses according to its maximum speed. Class 3a with a maximum speed of 120 km/h and class 3b with a maximum speed greater than 120 km/h. The cycle is divided into 4 driving categories, low, medium, high, and super high as shown in Figure 7.

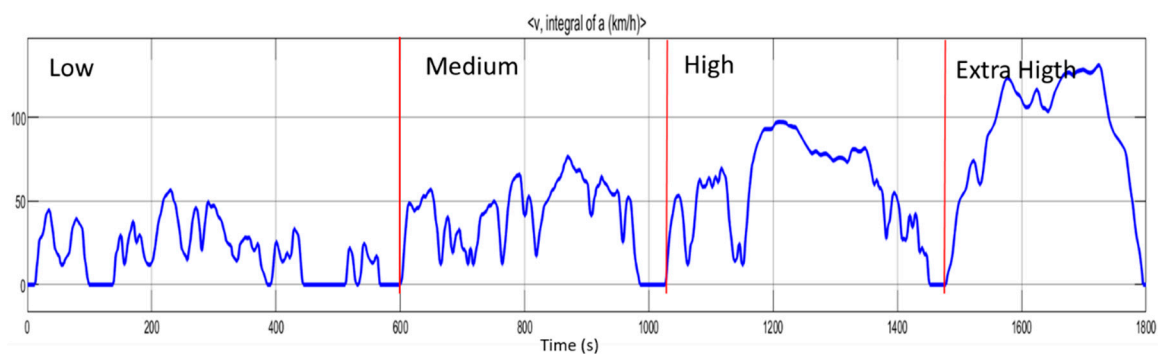


Figure 7. Worldwide Harmonised Light Vehicles Test Procedure (WLTP) cycle for class 3b vehicles.

### 2.4. Road Roughness

There are currently two main methods for measuring road roughness. The first one obtains the power distribution over different frequencies at which the signal is formed. It can be used to create an artificial road profile and to characterize the test road segment. The second one is the International Roughness Index (IRI).

To simulate the vibration generated by the road roughness, the road profile is obtained through the methodology established by ISO 8608 2016 [36]. According to this methodology, road roughness can be classified from a very good condition (A) to a very bad condition (H). In our case, a medium type C classification road was selected. A random road profile is generated through a unit input signal of white noise filtered using a low pass filter as follows:

$$G(s) = \frac{2\pi n_0 \sqrt{G_q u}}{s + 2\pi f_0} \quad (44)$$

where  $G_q = 2.56 \times 10^{-6}$  m/cycle is a mean value according to the class C road roughness;  $u$  corresponds to the vehicle speed;  $n_0$  is the reference spatial equal to the value of  $0.1 \text{ m}^{-1}$ ; and  $f_0$  is the minimum cut-off frequency with a value of 0.0628 Hz.

Figure 8 shows the class of road type C obtained applying Equation (44).

Equation (44) is a transfer function that can be used to find the road roughness in the time domain (Equation (45)) [37,38]:

$$\dot{z}(t) = -2\pi f_0 z(t) + 2\pi \sqrt{G_q u(t)} w(t) \quad (45)$$

where  $z(t)$  is the road roughness and  $w(t)$  is a white Gaussian noise. The obtained road profile is shown in Figure 9 for a variable speed according to the WLTP cycle.

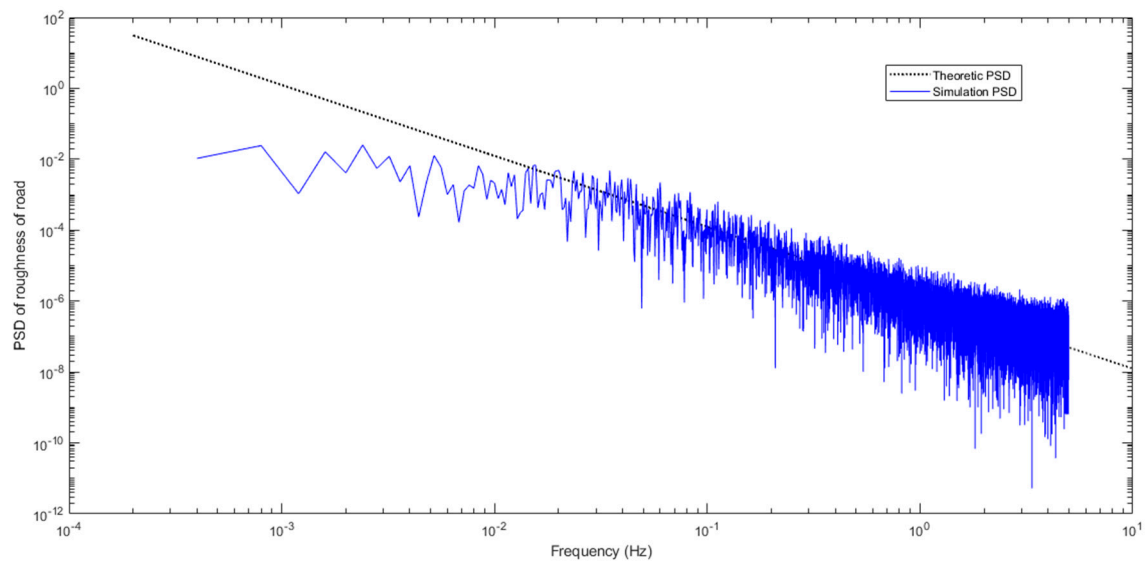


Figure 8. Displacement PSD (Power Spectral Density) for a type c road.

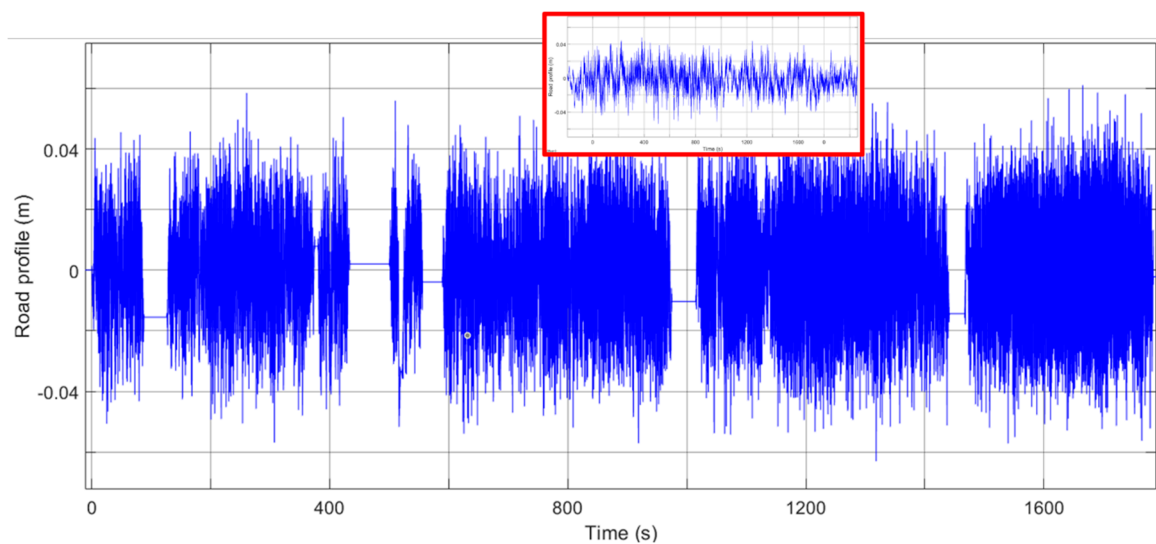
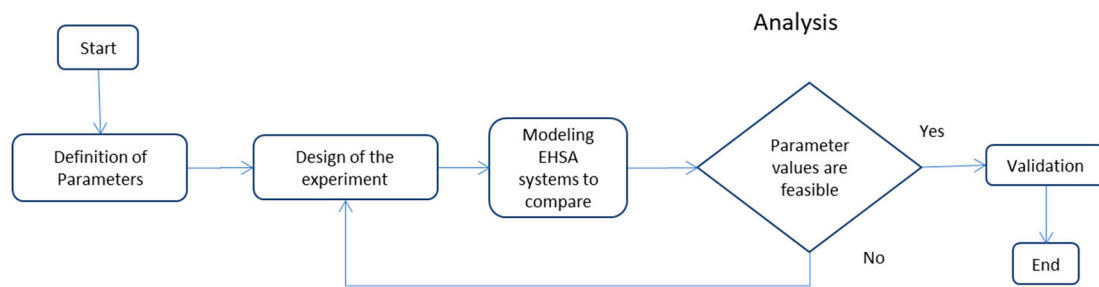


Figure 9. WLTP cycle with type c road profile.

This profile is applied to the 4 wheels of the vehicle model, with a delay between the front wheels of 0.1 s and 0.2 s between the rear wheels. In this way, pitch and roll modes of the vehicle model are excited.

### 3. Applied Methodology

Once the vehicle model is set up (9 DOF), the EHSA technologies are selected (BS-EHSA, RP-EHSA and CD-EHSA), and road profile (type C) and testing cycles (WLTP driving cycle) are chosen, it is time to apply the proposed methodology (Figure 10) to select the best design option. Regarding the design of the EHSA, different objectives can be selected, and the methodology can be adapted to them. In this case, the design is aimed at selecting the best EHSA technology to replace a real light vehicle suspension [32], where a fixed damping factor of 1500 Ns/m was set up. This objective is at the same time realistic and useful if one intends to introduce EHSA technology in real vehicles. Once the design can cope with the damping objective, it can be further optimised for maximum energy recovery.



**Figure 10.** Methodology Flowchart.

Based on this design objective, the three EHSA models are studied and geometrically adapted to achieve the damping objective.

The methodology will be applied according to the following flow chart.

Tables 2 and 3 show the characteristics of the generator and vehicle parameters to be used in the three EHSA models. According to our methodology, it is necessary to have the same testing conditions for our EHSA systems to be compared. We selected a motor whose parameters were used in the work reported by Lincoln [14], obtained from a commercial motor (Maxon Motor 218010) [39].

**Table 2.** The Generator parameters used in the three EHSA models.

Generator Parameters
$R_i$ (Ohms) = 6.6
$L$ (H) = $1.7 \times 10^{-3}$
$K_e$ (Vs/rad) = 0.137
$K_i$ (Nm/A) = 0.137
$J_g$ ( $\text{kg}\cdot\text{m}^2$ ) = $121 \times 10^{-5}$

**Table 3.** The commons vehicle parameters used in the three EHSA models.

Vehicle Parameters
$m_2$ (Kg) = 650
$m_1$ (Kg) = 24
$I_{2xz}$ ( $\text{Kg}\cdot\text{m}^2$ ) = 77
$I_{2yz}$ ( $\text{Kg}\cdot\text{m}^2$ ) = 270
$k_2$ (N/m) = 10,286
$H$ (mm) = 900
$a$ (mm) = 1110
$b$ (mm) = 1227

### 3.1. Case I. BS-EHSA

Modelling conditions for each EHSA system are shown in Figure 1.

Based on Equation (17), the parameters that intervene in the calculation of the damping are identified. To determine which of those parameters have greater influence within the system, a design of experiments (DOE) was carried out. The results of this study show the relative influence of the screw lead, the speed ratio of the gearbox and the external resistance (Figure 11):

Based on these results, we can modify some of these parameters to obtain the damping objective. The damping value of 1500 Ns/m can be obtained in different parameter combinations (Figure 12). In this case, resistance of 1 Ohm and 8 mm lead screw were selected due to the market availability.

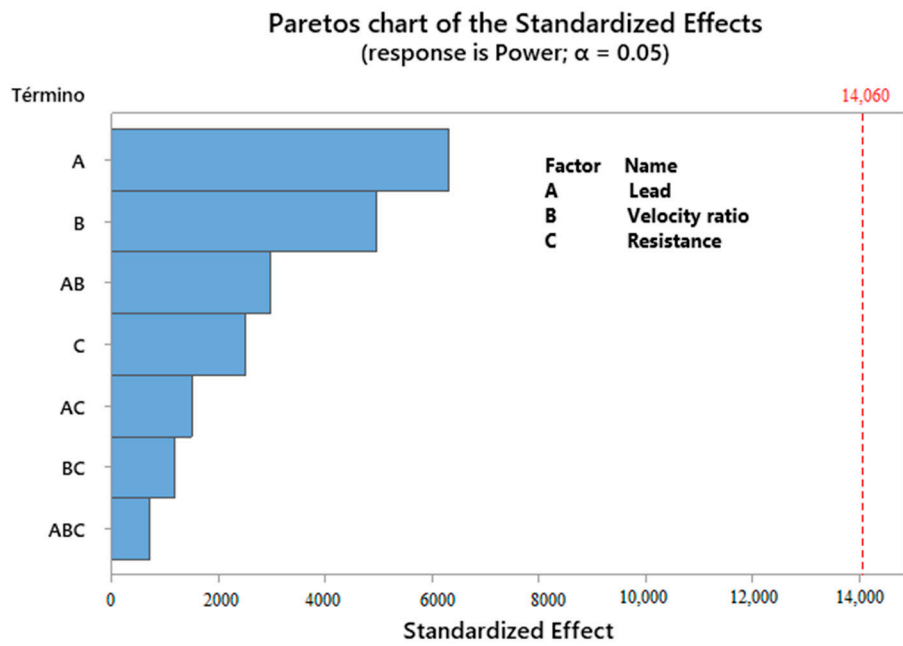


Figure 11. Design of experiment (DOE) results to identify the parameters of the greatest effect.

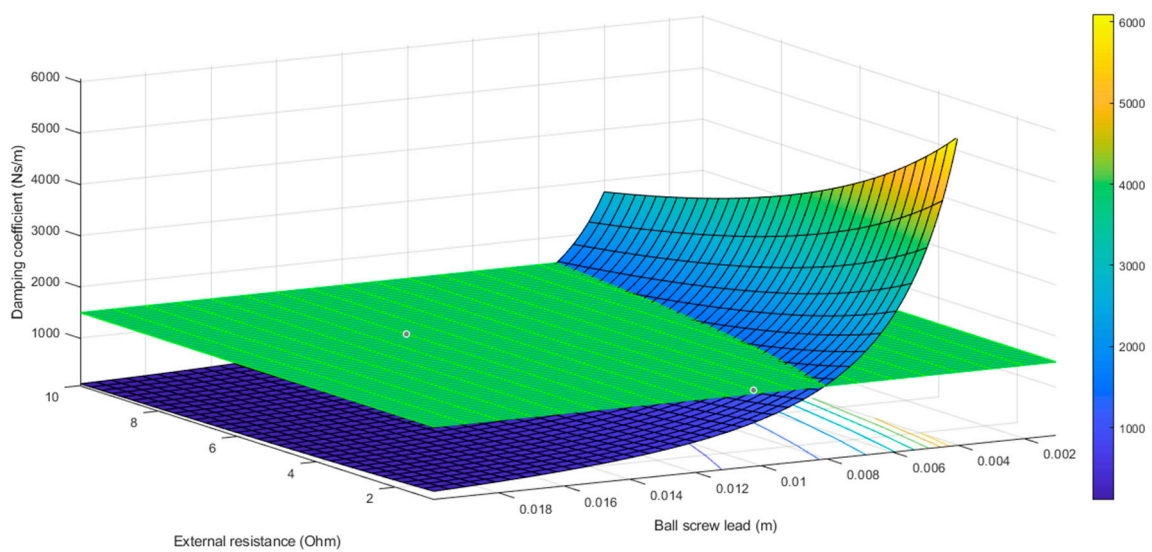


Figure 12. The plane cut with the value of 1500 Ns/m and the function in terms of resistance and screw lead.

Table 4 shows the parameters used for the ball screw model simulation according to the results obtained by DOE to reach the damping target value of 1500 Ns/m.

Table 4. EHSA ball screw system parameters.

Parameters of the Ball Screw Simulation	Name	Value	Units
Spindle inertia	$J_s$	180	$g\text{ cm}^2$
Screw lead	$l$	8	mm
Transmission factor of the multiplier	$k_{mu}$	1	-
External resistance	$R_e$	1	$\Omega$

3.2. Case II. RP-EHSA

The same process was followed (Figure 1) with the rack and pinion system. A DOE study showed the most influencing parameters (Figure 13).

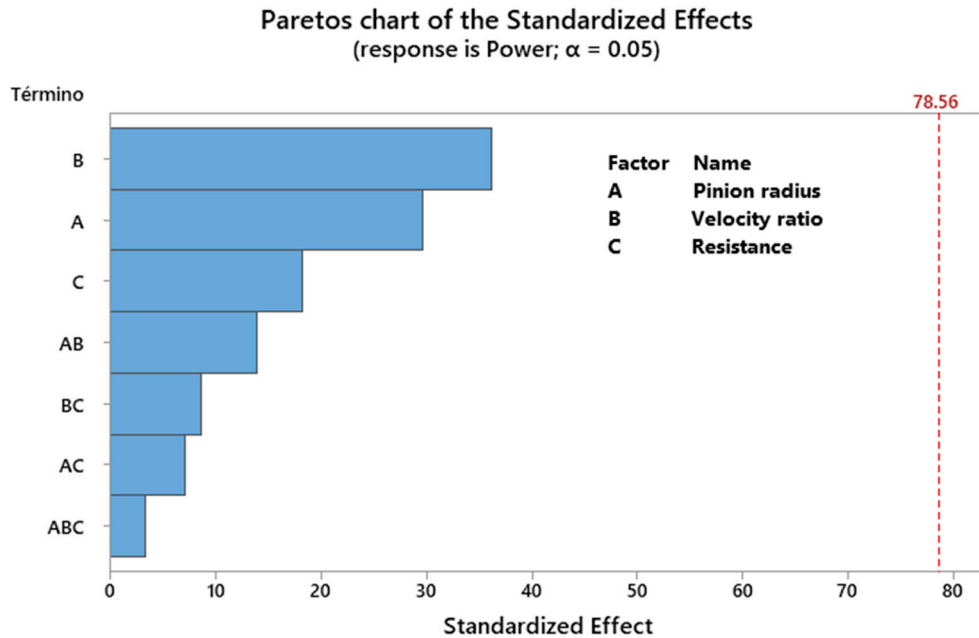


Figure 13. DOE results to identify parameters of the greatest effect.

Figure 14 shows the surface area of the external resistance values and the radius of the pinion vs. the damping.

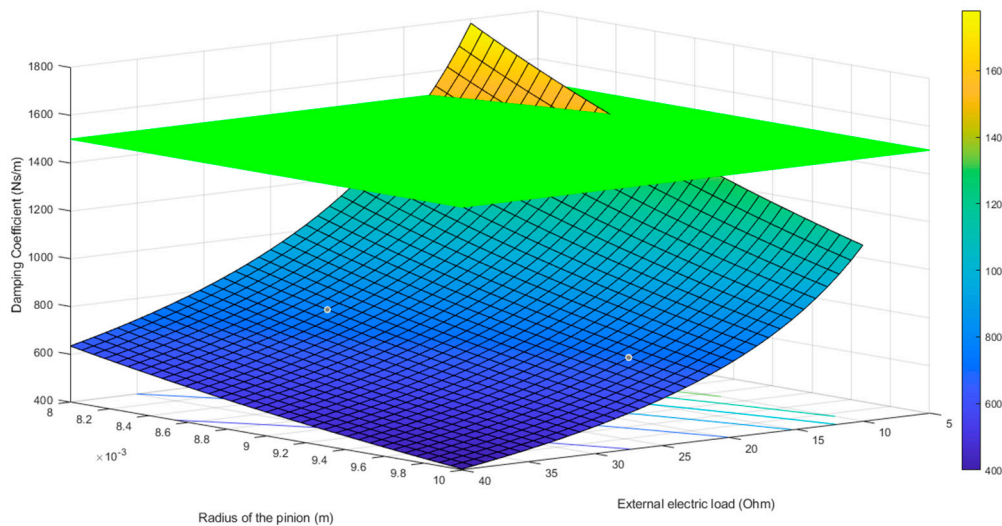


Figure 14. The cutoff plane is defined with a 1500 value of the damping coefficient, showing the possible values of resistance and radius of the pinion.

In this case, the combinations of  $r_p = 0.01$  m and  $R_e = 6$  Ohm were chosen.

Table 5 shows the parameter values used for the rack and pinion in the simulation according to the results obtained by DOE to reach the damping target value.

**Table 5.** EHSA rack and pinion system parameters.

Parameters of the Rack-Pinion Simulation	Name	Value	Units
Inertia of the gearbox	$J_{mu}$	37.5	$\text{g cm}^2$
Pinion inertia	$J_p$	192	$\text{g cm}^2$
Pinion radius	$r_p$	0.01	m
Gearbox transmission factor	$k_{mu}$	10	-
Resistance externa	$R_e$	6	$\Omega$

### 3.3. Case III. CD-EHSA

In this case, the methodology is applied to the CD-EHSA; following the same structure as it was shown in Figure 1.

Based on Equation (27), the damping of the cable transmission system depends on several parameters. To analyse their influence, a DOE study is also carried out on them (Figure 15).

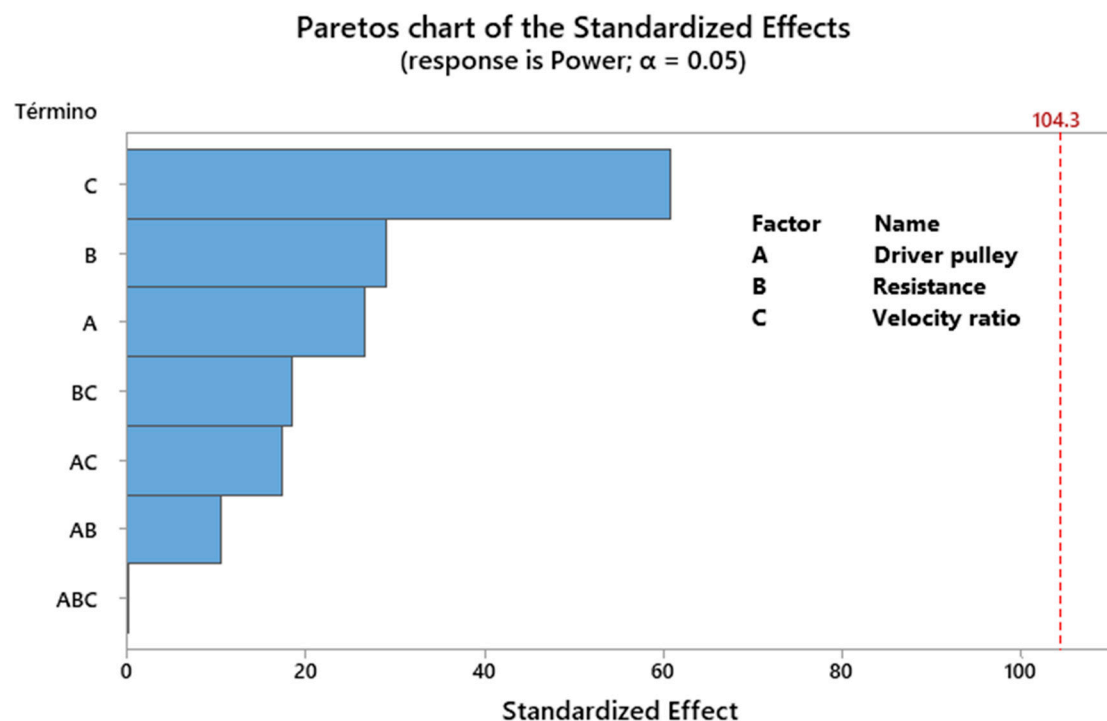


**Figure 15.** DOE results to identify the parameters of the greatest effect.

Figure 16 shows the values of the effect of the external resistance and the radius of the drive pulley concerning the damping.

In this case, due to construction availability, the selected combination of an external resistance of 22 ohms and a pulley radius of 0.008 m was preferred.

Table 6 shows the parameters of the cable transmission system used in the simulation according to the results obtained by DOE to reach the damping target value of 1500 Ns/m.

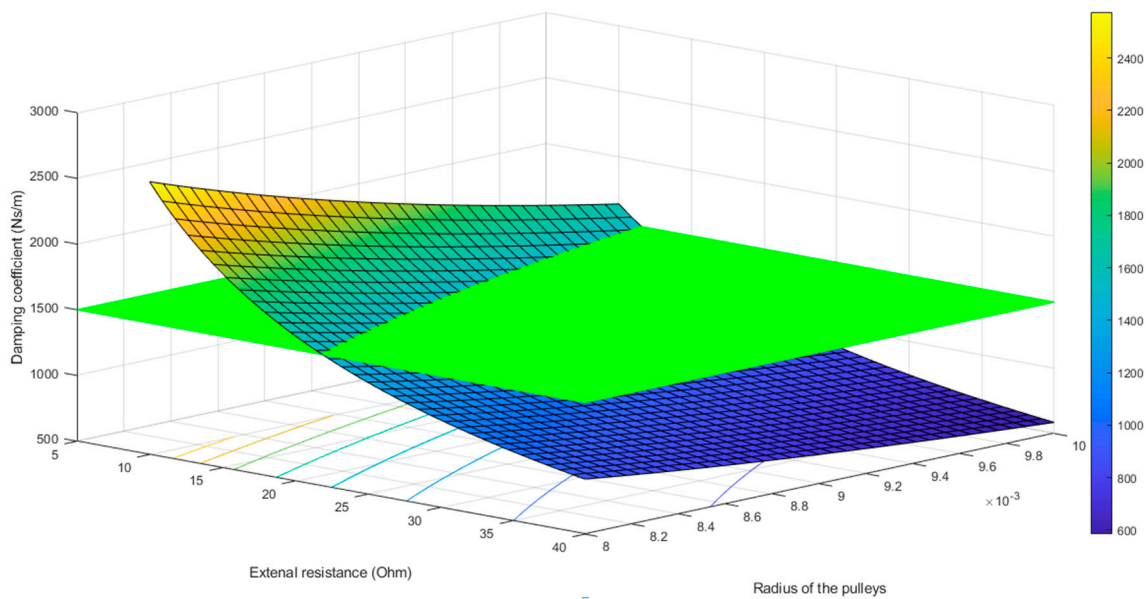


**Figure 16.** The cut of the plane with the value of 1500 Ns/m and the plane with the values of resistance and radius of the pinion.

**Table 6.** Parameters of the EHSA cable transmission system.

Parameters of the Cable Transmission Simulation	Name	Value	Units
Inertia of the multiplier	$J_{mu}$	100	$\text{g cm}^2$
Drive Pulley Inertia	$J_{pt1}$	81	$\text{g cm}^2$
Inertia of the driven pulley	$J_{pt2}$	81	$\text{g cm}^2$
Cable stiffness coefficient	$k_c$	1104	$\text{KN/m}$
Pulley radius	$R_{pl} = R_{pg}$	8	mm
Cable damping coefficient	$c_c$	100	$\text{N/(m/s)}$
Gearbox transmission factor	$k_{mu}$	12	-
External resistance	$R_e$	22	$\Omega$

#### 4. Results and Discussion

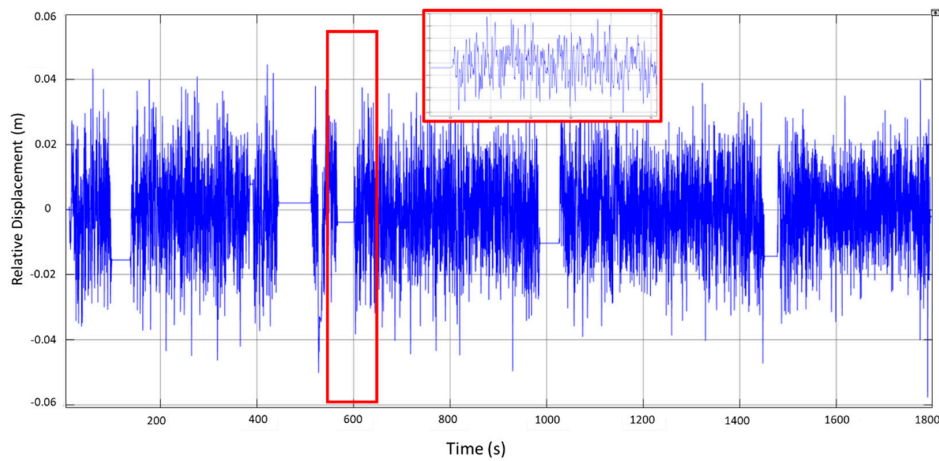
From the results obtained above, it was possible to limit the universe of combinations to achieve the damping objective value (1500). The three EHSA technologies were tested in a WLTP driving cycle, combined with a type of road C. The parameter selection in each ESHA model focused on those values that were functional from the practical point of view, seeking to have the least number of elements and to reduce the weight of the system. The selection of the parameters was based on DOE studies as in Figures 11, 13 and 15.

In the first case, the BS-EHSA system in Figure 12 presented a wide range of possible combinations. However, to make the system functional, the parameters were reduced to integer values where a balance between efficiency and feasible ball screw lead was chosen.

In the second case, the RP-EHSA system was studied (Figure 14). The system was very sensitive to changes in the radius of the pinion and the external resistance. However, to reach the damping target value, it was necessary to incorporate an external gearbox.

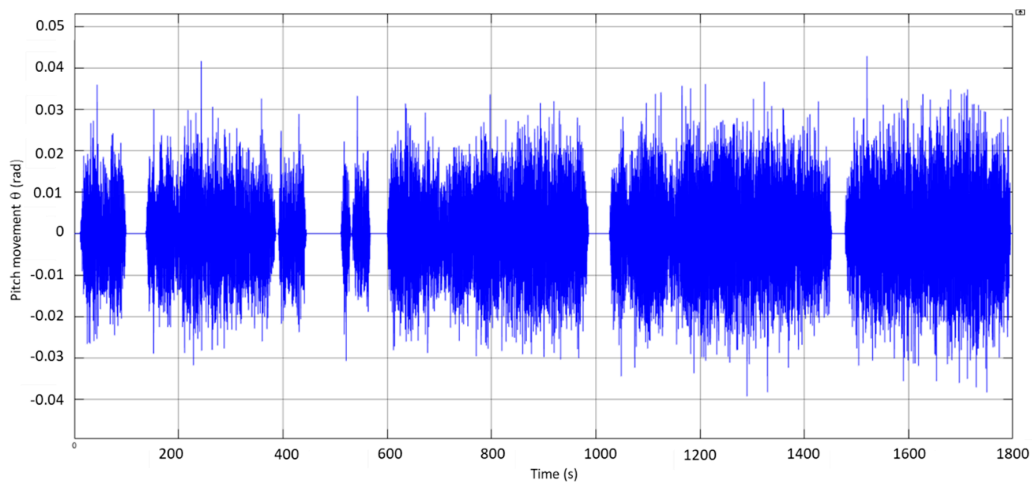
In the third case, the CD-EHSA system showed many possible solutions (see Figure 16). The solution was narrowed by looking for the smallest pulley diameter to have the best speed ratio combined with a multiplier gearbox with a minimum speed ratio.

Comparing the results of the road profile (Figure 9) vs. the displacement of the suspended mass (Figure 17) is evident the damping in the sprung mass.



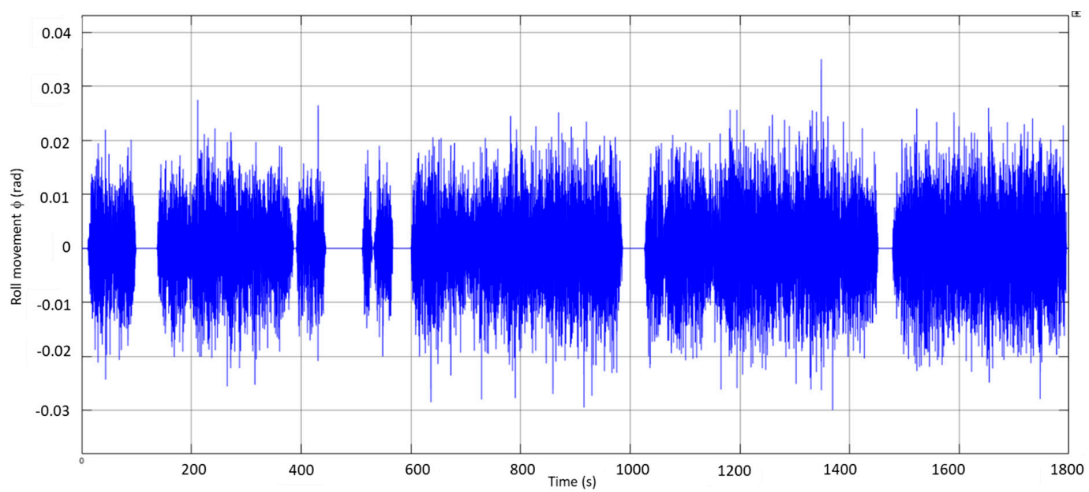
**Figure 17.** Bounce displacement of the sprung mass.

Figure 18 shows the pitch angles derived from the input time delays at each wheel corner.



**Figure 18.** The angular displacement of the pitch.

Figure 19 shows the roll angle derived from the delays (Figure 20) at each wheel corner.



**Figure 19.** The angular displacement of the turns.

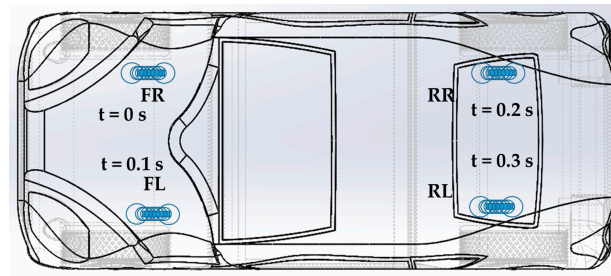


**Figure 20.** Top view of shock absorber position labels, where *FL* is Front Left, *FR* is Front Right, *RL* is Rear Left, *RR* is Rear Right, *t* is the delay time.

The sequence of road input values presented to each shock absorber in the simulation is shown in Figure 20.

In these conditions, energy was recovered for each of the EHSA systems from the WLTP drive cycle on each wheel. Figures 21–23 show the values of each shock absorber without considering the full-stop times in the driving cycle. We start by comparing the four wheels shown the energy recovered by the BS-EHSA Figure 21.

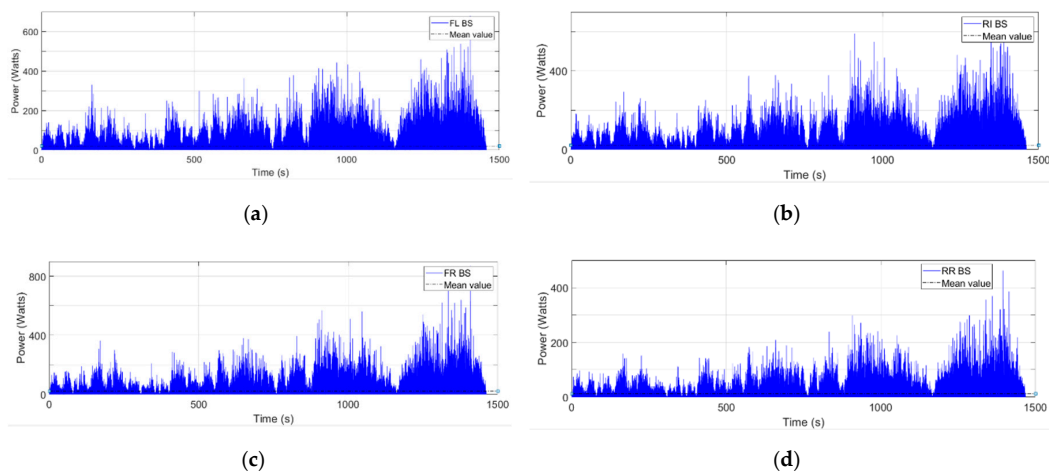


**Figure 21.** Average energy recovery values per shock absorber from the driving cycle for each EHSA BS system, (a)  $\bar{P} = 20.42$  W Front Left (FL), delay 0 s, (b)  $\bar{P} = 21.75$  W Rear Left (RL), delay 0.2 s, (c)  $\bar{P} = 22.55$  W Front Right (FR), delay 0.1 s, (d)  $\bar{P} = 24.86$  W Rear Right (RR), delay 0.3 s.

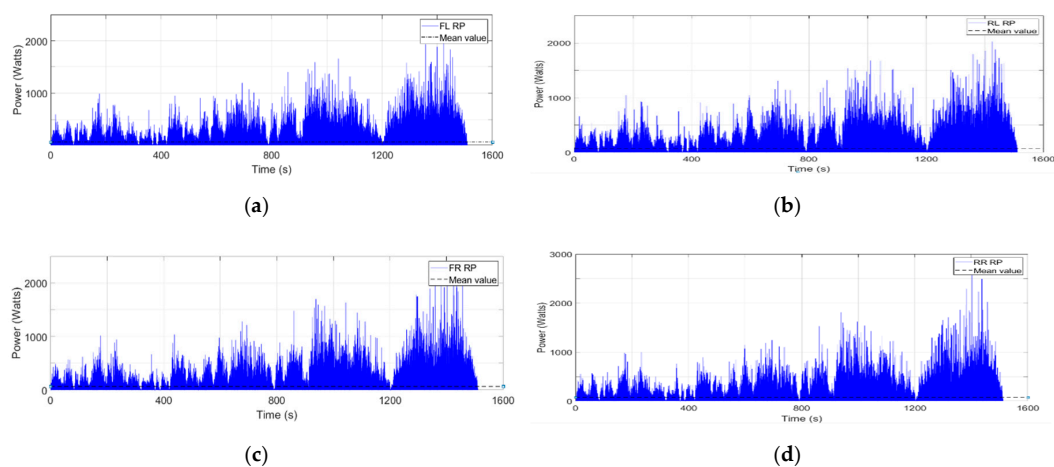


**Figure 22.** Average energy recovery values per shock absorber from the driving cycle for each EHSA RP system. (a)  $\bar{P} = 67.83$  W Front Left (FL), delay 0 s, (b)  $\bar{P} = 70.99$  W Rear Left (RL), delay 0.2 s, (c)  $\bar{P} = 70.68$  W Front Right (FR), delay 0.01 s, (d)  $\bar{P} = 73.88$  W Rear Right (RR), delay 0.3 s.

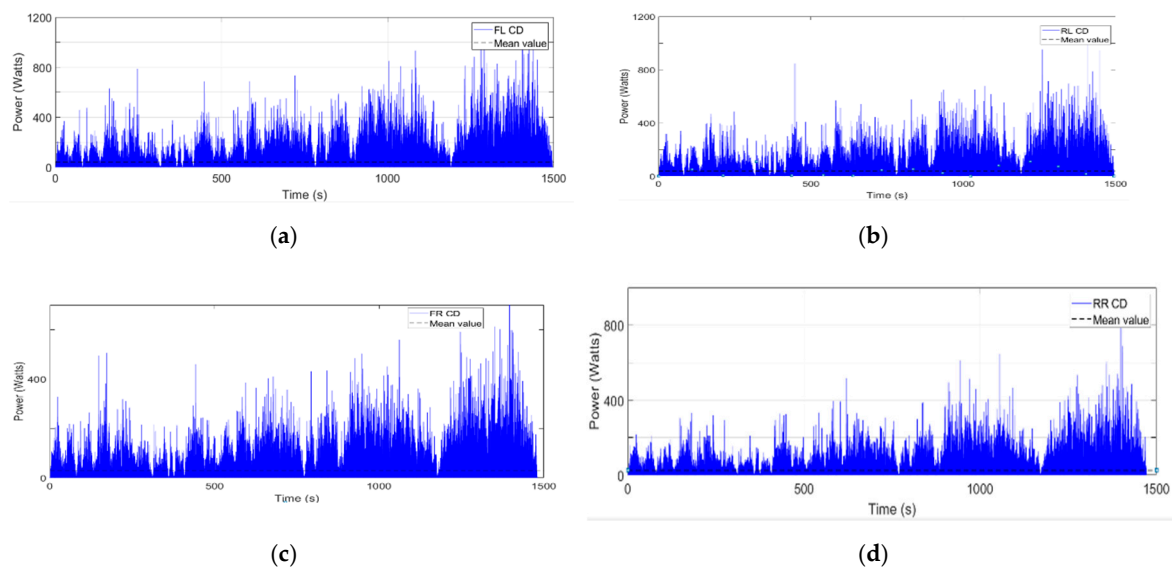


**Figure 23.** Average energy recovery values per shock absorber from the driving cycle for each EHSA CD system. (a)  $\bar{P} = 41.85$  W Front Left (FL), delay 0 s, (b)  $\bar{P} = 38.46$  W Rear Left (RL), delay 0.2 s, (c)  $\bar{P} = 27.20$  W Front right (FR), delay 0.1s, (d)  $\bar{P} = 25.12$  W Front right (FR), delay 0.3 s.

From the results obtained for the BS-EHSA, a total average harvest of  $\overline{P_{Tave}} = 89.58$  Watts was obtained.

The values obtained for the EHSA rack and pinion system are shown in Figure 22.

From the results obtained for the RP-EHSA, a total average harvest of  $\overline{P_{Tave}} = 283.38$  W was obtained, with the highest value of energy recovered. This system uses a multiplier with a speed ratio of 1:10, which supports a higher value than the ball screw system.

The values obtained for the last CD-EHSA system are shown in Figure 23.

From the results obtained for the CD-EHSA (Figure 23), a total average energy harvesting of  $\overline{P_{Tave}} = 132.63$  Watts was obtained, being the second-best. This system uses a multiplier with a speed ratio of 1:12 (Table 6), which supports a higher value than the BS-EHSA system but lower than the RP-EHSA systems.

## 5. Conclusions

After reviewing the relevant literature, it is clear that there are different technologies used in EHSA. It is also clear that each author designs, develops, simulates and validates these systems in a different way than those with similar systems or technologies. This paper presented a methodology that can compare the performance of different EHSA technologies against a common design objective. Specifically, a given damping coefficient was set as a design objective, corresponding to that of a real vehicle, with the challenge of achieving a functional EHSA shock absorber with each of the chosen EHSA technologies. It is shown that the methodology is general and applicable to any type of EHSA. In this case, it was applied to two of the most used EHSAs in the literature (Ball Screw and Rack and Pinion) and a little-known one based on cable dynamics, which validates its versatility.

Therefore, three different EHSA technologies with different characteristics were compared to obtain a given damping factor. The same methodology was applied to the three EHSA technologies (with different design parameters), simulating a given drive cycle, a light-duty vehicle, and a specific road roughness profile producing normalized inputs.

The selection of the EHSA parameters was based on those with the greatest effect on damping, which were simulated with the mathematical modelling of the EHSA system and with a design of experiments.

Once the damping objective was achieved for each EHSA technology, the energy recovered was calculated in each system. Given these results, the highest average instantaneous energy recovered is the RP-EHSA system with the value of  $\overline{P_{Tave}} = 283.38$  Watts, followed by the CD-EHSA system with  $\overline{P_{Tave}} = 132.63$  Watts, and finally, the BS-EHSA system with  $\overline{P_{Tave}} = 89.58$  Watts. These results assure that each of the technologies achieves the objective damping factor. In this regard, the BS-EHSA was able to reach the damping factor with no gearbox. On the other hand, the RP-EHSA and the CD-EHSA systems require a gearbox to hit that damping value. The BS-EHSA system is the simplest design and does not add extra weight to the car that will, eventually, affect fuel consumption and represents higher costs. In this regard, the presented methodology has proven helpful to compare three different EHSA technologies for a given design objective with a fixed damping ratio.

Therefore, using this methodology, it is possible to compare different EHSA technologies under the same testing conditions regarding vehicle model, road profile, driving cycle and so on. Design objectives can vary from one case to another, but they can be reliably compared.

In future studies, different objective parameters should be considered, balancing the energy recovered and the weight and cost of the total system.

**Author Contributions:** Performed the state-of-the-art analysis, J.L.O. and C.G.-R.; conceived the methodology proposal, J.L.O. and C.G.-R.; modelling and simulation, C.G.-R.; obtained the funding, J.L.O.; investigation, writing and revisions, C.G.-R. and J.L.O.; supervision, J.L.O.; validation, C.G.-R.; the analysis of the data was done by C.G.-R., and J.L.O.; the artwork was prepared by C.G.-R. All authors have read and agreed to the published version of the manuscript.

**Funding:** The authors thank the Global Nebrija-Santander Chair of Energy Recovery in Surface Transport for their financial support. This work was also supported by the Comunidad de Madrid [grant SEGVAUTO 4.0-CM-P2018EEMT-4362] and the Agencia Estatal de Investigación [grant RETOS 2018-RTI2018-095923-B-C22].

**Conflicts of Interest:** The authors declare no conflict of interest.

## Nomenclature

$\theta_p, \dot{\theta}_p, \ddot{\theta}_p$	Angular displacement: angular velocity and, angular acceleration of pinion
$\theta_{pg}, \dot{\theta}_{pg}, \ddot{\theta}_{pg}$	Pulley angular displacement, angular velocity and, angular acceleration
$k_e$	Back electromotive voltaje constant
$k_t$	Back electromotive force coefficient
$\omega$	Frecuency
$R$	Total resistance
$C_{EHSA1,2,3,4}$	Damping of EHSA systems
$\phi$	Roll mode angle
$I_{2xx}$	Moment of inertia of sprung mass
$I_{2yy}$	Moment of inertia of sprung mass
$k_{01,02,03,04}$	Tire stiffness
$K_{1,2,3,4}$	Stiffness of suspensions
$L_B$	Back length
$L_F$	Frontal length
$L_L$	Left length
$L_R$	Rigth length
$m_{1,2,3,4}$	Unsprung mass
$M_2$	Sprung mass
$\theta$	Pitch mode angle
$Z_2$	Vertical displacement of shock absorber
$z_1, \dot{z}_1, \ddot{z}_1$	Vertical displacement, velocity and acceleration of sprung mass
$L$	Generator inductance
$R_i$	Internal generator resistance
$R_e$	External resistance
$i$	Current of the conductor

$k_i$	Constant of the torque
$\tau_i$	Output torque of the motor
$\tau_g$	Generator input torque
$J_g$	Generator inertia
$\alpha_g$	Spindle rotation
$U_{emf}$	Counter electromotive force
$k_e$	Back electromotive force coefficient
$K_g$	Stiffness equivalent factor
$C_{eq}, C_{eqRP}, C_{eqCD}$	Damping equivalent factors (ball Screw, rack-pinion and cable dynamic)
$C_g$	Generator damping equivalent factors
$\eta_{bs}$	Ball screw efficiency
$F_a$	Equivalent force for suspension configurations
$l$	lead ball screw
$\dot{\alpha}_s, \ddot{\alpha}_s, \ddot{\alpha}_s$	Ball Screw angular, displacement, velocity and, acceleration
$m_{eq}, m_{eqRP}, m_{eqCD}$	Equivalent mass for ball Screw, rack-pinion and, cable dynamic
$c_{eq}$	Equivalent damping for ball Screw
$k_{eq}, k_{eqRP}, k_{eqCD}$	Equivalent stiffness for ball screw, rack and pinion and, cable dynamic
$k_g$	Equivalent stiffness for generator
$J_s$	Screw inertia
$r_p$	Pinion radius
$\tau_{mu}$	Pinion torque
$\theta_{mu}, \dot{\theta}_{mu}, \ddot{\theta}_{mu}$	Gearbox torque
$\tau_p$	Gearbox angular displacement, angular velocity and, angular acceleration
$\eta_p$	Efficiency of the rack-pinion
$k_{mu}$	Gearbox ratio
$J_{mu}$	Gearbox inertia
$T_1, T_2, T_3$	Cable tension
$k_c$	Cable stiffness
$R_{pl}, R_{pg}$	Pulley radius
$c_c$	Cable damping
$\tau_{pg}$	Pulley torque
$\eta_{pt1}, \eta_{pt2}$	Pulley efficiency
$\eta_{pg}$	Generator efficiency
$\eta_{mu}$	Gearbox efficiency
$J_{pl}, J_{pg}$	Pulley inertia
$G_q$	Road displacement
$n_o$	Reference spatial frequency
$G_q$	Road roughness coefficient
$f_o$	Minimum cut-off frequency
$n$	Vehicle speed
$\omega(t)$	White Gaussian noise

## References

1. EPA (Environmental Protection Agency). The EPA Automotive Trends Report. Available online: <https://nepis.epa.gov/Exe/ZyPDF.cgi?Dockkey=P100YVK3.pdf> (accessed on 10 January 2020).
2. EPA (Environmental Protection Agency). The Official U.S. Government Source for Fuel Economy Information. Available online: <https://www.fueleconomy.gov/feg/atv-ev.shtml> (accessed on 10 January 2020).
3. European Commission. Comunicación de la Comisión al Parlamento Europeo, al Consejo, al Comité Económico y Social Europeo y al Comité de las Regiones, UE. Available online: <https://ec.europa.eu/transparency/regdoc/rep/1/2016/ES/COM-2016-501-F1-ES-MAIN-PART-1.PDF> (accessed on 18 January 2020).
4. Zuo, L.; Zhang, P.-S. Energy Harvesting, Ride Comfort, and Road Handling of Regenerative Vehicle Suspensions. *J. Vib. Acoust Trans. ASME* **2013**, *135*, 1–8. [CrossRef]

5. Bowen, L. Estudio Teórico-Experimental de Sistemas de Recuperación de Energía en la Suspensión de un Vehículo Automóvil. Ph.D. Thesis, Universidad de Nebrija, Madrid, Spain, 2018; p. 156.
6. Zou, J.; Guo, X.; Xu, L.; Tan, G.; Zhang, C.; Zhang, J. Design, Modeling, and Analysis of a Novel Hydraulic Energy-Regenerative Shock Absorber for Vehicle Suspension. *Shock. Vib.* **2017**, *2017*, 1–12. [[CrossRef](#)]
7. Sultoni, A.I.; Sutantra, I.N.; Pramono, A.S. Modeling, Prototyping and Testing of Regenerative Electromagnetic Shock Absorber. *Appl. Mech. Mater.* **2014**, *493*, 395–400. [[CrossRef](#)]
8. Gysen, B.L.J.; Van Der Sande, T.P.J.; Paulides, J.J.H.; Lomonova, E.A. Efficiency of a Regenerative Direct-Drive Electromagnetic Active Suspension. *IEEE Trans. Veh. Technol.* **2011**, *60*, 1384–1393. [[CrossRef](#)]
9. Li, Z.; Zuo, L.; Luhrs, G.; Lin, L.; Qin, Y.-X. Design, Modeling, and Road Tests of Electromagnetic Energy-Harvesting Shock Absorbers. In Proceedings of the ASME 2012 5th Annual Dynamic Systems Control Conference Joint with JSME 2012 11th Motion and Vibration Conference, Fort Lauderdale, FL, USA, 17–19 October 2012; Volume 3, pp. 675–684.
10. Zhang, Z.; Zhang, X.; Chen, W.; Rasim, Y.; Salman, W.; Pan, H.; Yuan, Y.; Wang, C. A high-efficiency energy regenerative shock absorber using supercapacitors for renewable energy applications in range extended electric vehicle. *Appl. Energy* **2016**, *178*, 177–188. [[CrossRef](#)]
11. Li, Z. Regenerative Shock Absorbers for Energy Harvesting. Master's Thesis, Mechanical Engineering, Stony Brook University, New York, NY, USA, August 2012.
12. Liu, Y.; Xu, L.; Zuo, L. Design, Modeling, Lab, and Field Tests of a Mechanical-Motion-Rectifier-Based Energy Harvester Using a Ball-Screw Mechanism. *IEEE/ASME Trans. Mechatron.* **2017**, *22*, 1933–1943. [[CrossRef](#)]
13. Maravandi, A.; Moallem, M. Regenerative Shock Absorber Using a Two-Leg Motion Conversion Mechanism. *IEEE/ASME Trans. Mechatron.* **2015**, *20*, 2853–2861. [[CrossRef](#)]
14. Bowen, L.; Vinolas, J.; Olazagoitia, J.L.; Otero, J.E. An Innovative Energy Harvesting Shock Absorber System Using Cable Transmission. *IEEE/ASME Trans. Mechatron.* **2019**, *24*, 689–699. [[CrossRef](#)]
15. Khoshnoud, F.; Zhang, Y.; Shimura, R.; Shahba, A.; Jin, G.; Pissanidis, G.; Chen, Y.K.; De Silva, C.W. Energy Regeneration from Suspension Dynamic Modes and Self-Powered Actuation. *IEEE/ASME Trans. Mechatron.* **2015**, *20*, 2513–2524. [[CrossRef](#)]
16. Wei, C.; Taghavifar, H. A novel approach to energy harvesting from vehicle suspension system: Half-vehicle model. *Energy* **2017**, *134*, 279–288. [[CrossRef](#)]
17. Lafarge, B.; Cagin, S.; Curea, O.; Hacala-Perret, A. From functional analysis to energy harvesting system design: Application to car suspension. *Int. J. Interact. Des. Manuf.* **2015**, *10*, 37–50. [[CrossRef](#)]
18. Nakano, K. Combined Type Self-Powered Active Vibration Control of Truck Cabins. *Veh. Syst. Dyn.* **2004**, *41*, 449–473. [[CrossRef](#)]
19. Mi, J.; Xu, L.; Zuo, L.; Zhu, Z.; Zuo, L. Design, modeling and testing of a one-way energy harvesting backpack. In Proceedings of the Spie Smart Structures and Materials + Nondestructive Evaluation and Health Monitoring, Denver, CO, USA, 4–8 March 2018.
20. Pham, T.; Jacob, J.; Wilkins, S.; Lauwerys, C.; Dhaens, M. Integrated model for battery Electric Vehicles with energy harvesting active suspension system. In Proceedings of the 12th International Conference on Ecological Vehicles Renewable Energies (EVER 2017), Monte Carlo, Monaco, 11–13 April 2017.
21. Abdelkareem, M.A.; Xu, L.; Guo, X.; Ali, M.K.A.; Elagouz, A.; Hassan, M.A.; Essa, F.; Zou, J. Energy harvesting sensitivity analysis and assessment of the potential power and full car dynamics for different road modes. *Mech. Syst. Signal Process.* **2018**, *110*, 307–332. [[CrossRef](#)]
22. European Commission Mobility and Transport. Implementing the New CO2 Emissions and Fuel Consumption Test for Cars and Vans—The WLTP and the Correlation Procedure. Available online: [https://ec.europa.eu/clima/sites/clima/files/transport/vehicles/cars/docs/faq\\_wltp\\_correlation\\_en.pdf](https://ec.europa.eu/clima/sites/clima/files/transport/vehicles/cars/docs/faq_wltp_correlation_en.pdf) (accessed on 10 August 2019).
23. González-Oropeza, R. Los ciclos de manejo, una herramienta útil si es dinámica para evaluar el consumo de combustible y las emisiones contaminantes del auto transporte. *Ing. Investig. Tecnol.* **2005**, *6*, 147–162. [[CrossRef](#)]
24. Zhu, Q.; Ishitobi, M. Chaotic vibration of a nonlinear full-vehicle model. *Int. J. Solids Struct.* **2006**, *43*, 747–759. [[CrossRef](#)]
25. Syuhri, A.; Hadi, W.; Syuhri, S.N.H. Damping properties and energy evaluation of a regenerative shock absorber. *Int. J. Interact. Des. Manuf. (IJIDeM)* **2018**, *12*, 1385–1397. [[CrossRef](#)]

26. Chen, X.; Wang, Y.; Wang, W.; Zhu, J.; Sun, H. Analysis and design of a new type of close wheel drive system based on gear-linkage and using motor as dynamic absorber. *Zhendong yu Chongji/J. Vib. Shock* **2016**, *35*, 46–51.
27. Riese, C.; Stump, O.; Gauterin, F. Investigation of the energy recuperation potential of the damper system for a compact class passenger car. *Int. J. Veh. Des.* **2017**, *74*, 281. [[CrossRef](#)]
28. Abdelkareem, M.A.; Xu, L.; Ali, M.K.A.; El-Daly, A.-R.B.M.; Hassan, M.A.; Elagouz, A.; Bo, Y. Analysis of the prospective vibrational energy harvesting of heavy-duty truck suspensions: A simulation approach. *Energy* **2019**, *173*, 332–351. [[CrossRef](#)]
29. Hongbin, R.; Sizhong, C.; Zhicheng, W. Model of excitation of random road profile in time domain for a vehicle with four wheels. In Proceedings of the 2011 International Conference on Mechatronic Science, Electric Engineering and Computer (MEC 2011), Jilin, China, 9–22 August 2011; pp. 2332–2335.
30. Tyan, F.; Hong, Y.-F.; Tu, S.-H.; Jeng, W.S. Generation of random road profiles. *J. Adv. Eng.* **2009**, *4*, 151–156.
31. Múčka, P. Simulated Road Profiles According to ISO 8608 in Vibration Analysis. *J. Test. Eval.* **2017**, *46*, 20160265. [[CrossRef](#)]
32. Bowen, L.; Vinolas, J.; Olazagoitia, J.L. Methodology for comparing the functional performance of energy harvesting shock absorbers. *Int. J. Appl. Electromagn. Mech.* **2017**, *55*, 545–564. [[CrossRef](#)]
33. Zhang, Y.; Guo, K.; Wang, D.; Chen, C.; Li, X. Energy conversion mechanism and regenerative potential of vehicle suspensions. *Energy* **2017**, *119*, 961–970. [[CrossRef](#)]
34. Ball Screw Construction and Features. Available online: <https://www.tpa-us.com/ballscrews.html> (accessed on 5 August 2020).
35. The European Automobile Manufacturers' Association. Available online: <https://www.wltpfacts.eu/what-is-wltp-how-will-it-work/> (accessed on 7 September 2020).
36. ISO-8608. *International Standard 8608:2016 Mechanical Vibration—Road Surface Profiles—Reporting of Measured Data*; ISO: Geneva, Switzerland, 2016.
37. Goenaga, B.; Fuentes, L.; Mora, O. Evaluation of the methodologies used to generate random pavement profiles based on the power spectral density: An approach based on the international roughness index. *Ing. Investig.* **2017**, *37*, 49–57. [[CrossRef](#)]
38. He, L.; Qin, G.; Zhang, Y.; Chen, L. Non-stationary random vibration analysis of vehicle with fractional damping. In Proceedings of the International Conference on Intelligent Computation Technology and Automation (ICICTA 2008), Hunan, China, 20–22 October 2008; Volume 2, pp. 150–157.
39. Maxon Motor ibérica S.A.U., “Maxon,” Swiss. 2020. Available online: <https://www.maxongroup.es/maxon/view/content/index/> (accessed on 18 November 2020).

**Publisher’s Note:** MDPI stays neutral with regard to jurisdictional claims in published maps and institutional affiliations.



© 2020 by the authors. Licensee MDPI, Basel, Switzerland. This article is an open access article distributed under the terms and conditions of the Creative Commons Attribution (CC BY) license (<http://creativecommons.org/licenses/by/4.0/>).